ADVANCED MATERIALS
www.advmat.de

Terahertz and Infrared Plasmon Polaritons in $PtTe_2$ Type-II Dirac Topological Semimetal

Salvatore Macis, Annalisa D'Arco, Lorenzo Mosesso, Maria Chiara Paolozzi, Silvia Tofani, Luca Tomarchio, Pinaka Pani Tummala, Sara Ghomi, Veronica Stopponi, Eleonora Bonaventura, Chiara Massetti, Davide Codegoni, Andrea Serafini, Paolo Targa, Michele Zacchigna, Alessio Lamperti, Christian Martella, Alessandro Molle,* and Stefano Lupi*

Surface plasmon polaritons (SPPs) are electromagnetic excitations existing at the interface between a metal and a dielectric. SPPs provide a promising path in nanophotonic devices for light manipulation at the micro and nanoscale with applications in optoelectronics, biomedicine, and energy harvesting. Recently, SPPs are extended to unconventional materials like graphene, transparent oxides, superconductors, and topological systems characterized by linearly dispersive electronic bands. In this respect, 3D Dirac and Weyl semimetals offer a promising frontier for infrared (IR) and terahertz (THz) radiation tuning by topologically-protected SPPs. In this work, the THz-IR optical response of platinum ditelluride ($PtTe_2$) type-II Dirac topological semimetal films grown on Si substrates is investigated. SPPs generated on microscale ribbon arrays of $PtTe_2$ are detected in the far-field limit, finding an excellent agreement among measurements, theoretical models, and electromagnetic simulation data. The far-field measurements are further supported by near-field IR data which indicate a strong electric field enhancement due to the SPP excitation near the ribbon edges. The present findings indicate that the $PtTe_2$ ribbon array appears an ideal active layout for geometrically tunable SPPs thus inspiring a new fashion of optically tunable materials in the technologically demanding THz and IR spectrum.

1. Introduction

Surface plasmon polaritons (SPPs) are coupled electromagnetic and electronic collective excitations confined at a metal–dielectric interface.[1] SPPs present peculiar electromagnetic effects like a reduced wavelength and a local field enhancement versus exciting radiation. These features, providing optical tunability and control in specific spectral bandwidths, fostered widespread technological applications in the last decades spanning from nano-infrared (IR) and surface-enhanced Raman spectroscopies,[2] to sensing techniques.[3,4] Although conventional metals are the usual means to generate SPPs,[1] nonconventional conductors like transparent oxides,[5] high-T_c superconductors,[6–8] strongly-correlated oxides,[9,10] graphene,[11–13] were recently proven to host SPPs with tailored properties by design owing to their extreme sensitivity to doping, temperature, electric and magnetic fields.

S. Macis, A. D'Arco, L. Mosesso, M. C. Paolozzi, L. Tomarchio, S. Lupi
Department of Physics
Sapienza University
Piazzale Aldo Moro 5, Rome 00185, Italy
E-mail: salvatore.macis@uniroma1.it

S. Tofani
CNR-IMM
Unit of Rome
Via del Fosso del Cavaliere 100, Rome 00133, Italy

The ORCID identification number(s) for the author(s) of this article can be found under https://doi.org/10.1002/adma.202400554

DOI: 10.1002/adma.202400554

P. P. Tummala, S. Ghomi, E. Bonaventura, C. Massetti, A. Lamperti, C. Martella, A. Molle
CNR-IMM
via C. Olivetti 2, Agrate Brianza (MB) I-20864, Italy
E-mail: alessandro.molle@cnr.it

V. Stopponi, M. Zacchigna
CNR-IOM
Area Science Park Strada Statale 14, km 163,5, Basovizza, TS 34149, Italy

E. Bonaventura
Department of Materials Science
University of Milano-Bicocca
Via Cozzi, 55, Milan 20125, Italy

D. Codegoni, A. Serafini, P. Targa
STMicroelectronics
via C. Olivetti 2, Agrate Brianza (MB) I-20864, Italy

SPPs-driven optical tunability is particularly advantageous in order to modulate the electromagnetic properties in the technologically demanding THz and IR spectral regions.[11,13,14] In this respect, topological materials[15] hold a disruptive potential by virtue of the peculiar electrodynamics of their topologically protected fermions.[16,17] A first breakthrough in this direction was achieved by effectively tuning the terahertz (THz) SPP frequency in Topological Insulators (TIs) like Bi_2Se_3,[18,19] and accessing their non-linear optical response under excitation with a strong THz field in the MV/cm range.[20,21]

The portfolio of optically tunable topological materials has been recently expanded by the discovery of Weyl (WSMs) and Dirac (DSMs) semimetals.[22] As WSMs and DSMs host fermions that formally comply with the Weyl/Dirac quantum field equation in selected electronic band cross-points (termed Weyl/Dirac nodes), they can be regarded as a 3D analog of graphene. In DSMs (WSMs) a band near the Fermi energy E_F has a 3D degenerate (non-degenerate) node with linear dispersive bands.[23] In particular, the electronic energy-momentum dispersion of a DSM can be written as $E(k) = U(k) \pm T(k)$ where k is the angular momentum, $U(k)$ and $T(k)$ are the potential and kinetic energy components, respectively. For a given k, if $U(k) > T(k)$, the Dirac cone is overtilted along the k direction and the system is classified as a type-II DSM. In the type-I class instead, the Dirac cone is not overtilted.[23–26] Type-I Dirac fermions have been discovered in Na_3Bi and Cd_3As_2,[15] whereas type-II ones can be found in the transition-metal dichalcogenides (TMDs).[23,27] While in TIs the relevant low energy dynamics occur in topologically protected surface states that are highly vulnerable to environmental and configurational conditions, DSMs (and WSMs) exhibit a more robust 3D topological texture thereby holding promise for a hugely stronger light–matter interaction in the THz and IR energy range as due to both the high electron mobility at room temperature (RT) and the inherent linear band dispersion near the Dirac (Weyl) nodes.[28] On this basis, DSMs (and WSMs) offer an unprecedented platform for engineering room temperature (RT) stable and tunable SPPs that are readily applicable to optoelectronic and photonic devices like optical modulators and photodetectors.[16]

THz and IR responsivity were reported in the bulk state of diverse TMDs with type-II DSM and WSM character.[29,30] Particularly appealing is the emerging class of transition metal ditellurides (TMTs) as host materials of type-II Dirac fermions because of the Te-induced increase of their spin-orbit splitting interaction.[27,31–34] The synthetic reduction of these materials in the state of ultra-thin film on substrate would be highly demanding to enable integration into a read-out integrated optoelectronic circuit platform. As a flagship material of this fashion, here we report on the synthesis of type-II Dirac platinum ditelluride ($PtTe_2$) film on Si-based substrates and their optical characterization in the THz-IR range. Here, we present an innovative procedure to fabricate $PtTe_2$ "plasmonic" microstructures, in the form of a microscale ribbon array, targeting the generation of geometrically tunable SPPs in the THz and IR regimes. SPP excitations are effectively excited in the far-field limit when the light polarization is perpendicular to the ribbon array.[10] Having fabricated samples with different ribbon width W and periodicity $2W$, we were able to sample the energy/momentum dispersion of SPPs in $PtTe_2$ and thus elucidate the whole SPP dynamics in the spectral range from 2 to 30 THz. This result paves the way to full control of the SPP optical properties in the THz and IR spectral range.

2. Results

Large-area $PtTe_2$ film in the topological 1T crystal structure[27] was grown on commercial SiO_2/Si substrates via a tellurization-based process and then structurally and optically characterized. The main contribution to the electric conductivity and then to SPP dynamics in $PtTe_2$ comes from Dirac carriers,[23,27,35–37] whose topological nature has been confirmed by ARPES,[27,37] and inelastic electron scattering.[36] To analyze the crystal structure of the as-grown $PtTe_2$ film (sketch in **Figure 1a**), cross-section lamellas were prepared for investigation with an aberration-corrected scanning transmission electron microscope (HAADF-STEM) operating in high-angle annular dark-field. Figure 1b shows the parallel Pt planes along the (001) direction with an average distance of 0.5 Å in agreement with the literature,[38] (a more complete characterization of the material's crystal structure is included in Figures S4–S6, Supporting Information). The reflectance $R(\omega)$ of the as-grown (non-patterned) film was measured (see Figure 1c black curve) in a wide spectral range from THz to visible (VIS) using a Bruker Vertex 70 V Fourier-transform interferometer and a V770 JASCO spectrophotometer (see Methods). This reflectance spectrum shows an overall metallic (Drude) behavior with some superimposed peaks at ≈465, ≈810, and ≈1075 cm^{-1}, corresponding to the substrate SiO_2 capping-layer phonons.[39] The RefFIT software[40] was used to analyze the measured reflectance spectrum upon taking into account the optical properties of the silicon substrate and its SiO_2 capping layer (blue curve in Figure 1c), measured under the same experimental conditions. The bare reflectance of the film (as extracted from the RefFIT fitting) is represented in Figure 1c (orange curve). This reflectance is characterized by a broad Drude term superimposed to a mid-IR absorption centered ≈2500 cm^{-1} and to an interband electronic transition in the near-IR/VIS region. Through the fitting process (see "Experimental Section"), we obtain a Drude plasma frequency of ≈8000 cm^{-1} and a scattering rate Γ of 440 cm^{-1}. The optical properties of the as-grown $PtTe_2$ film have been used as input for the electromagnetic simulation of the patterned $PtTe_2$ films (see below Section 6, Supporting Information).

SPPs cannot be directly excited by electromagnetic radiation because their dispersion law is such as to prevent the conservation of momentum in the photon absorption process.[10] The necessary extra-momentum can be obtained by patterning the surface with a microstructure.[18]

The validation of the $PtTe_2$ growth process enabled us to develop a method for the fabrication of $PtTe_2$-based plasmonic gratings in the microscale. These ones are fabricated through a tellurization of prepatterned metallic stripes thereby resulting in geometrically controlled arrays of $PtTe_2$ microstripes with tunable size and periodicity.[41] Figure 1d and Figure S1 (Supporting Information) schematically depict the microfabrication process flow encompassing the annealing of Pt micro-ribbons in a tellurium-rich atmosphere to obtain a geometrically tunable array of $PtTe_2$ microribbons by pristine design.

The atomic force microscopy (AFM) topographies at the bottom of Figure 1d confirm that the lateral size of the

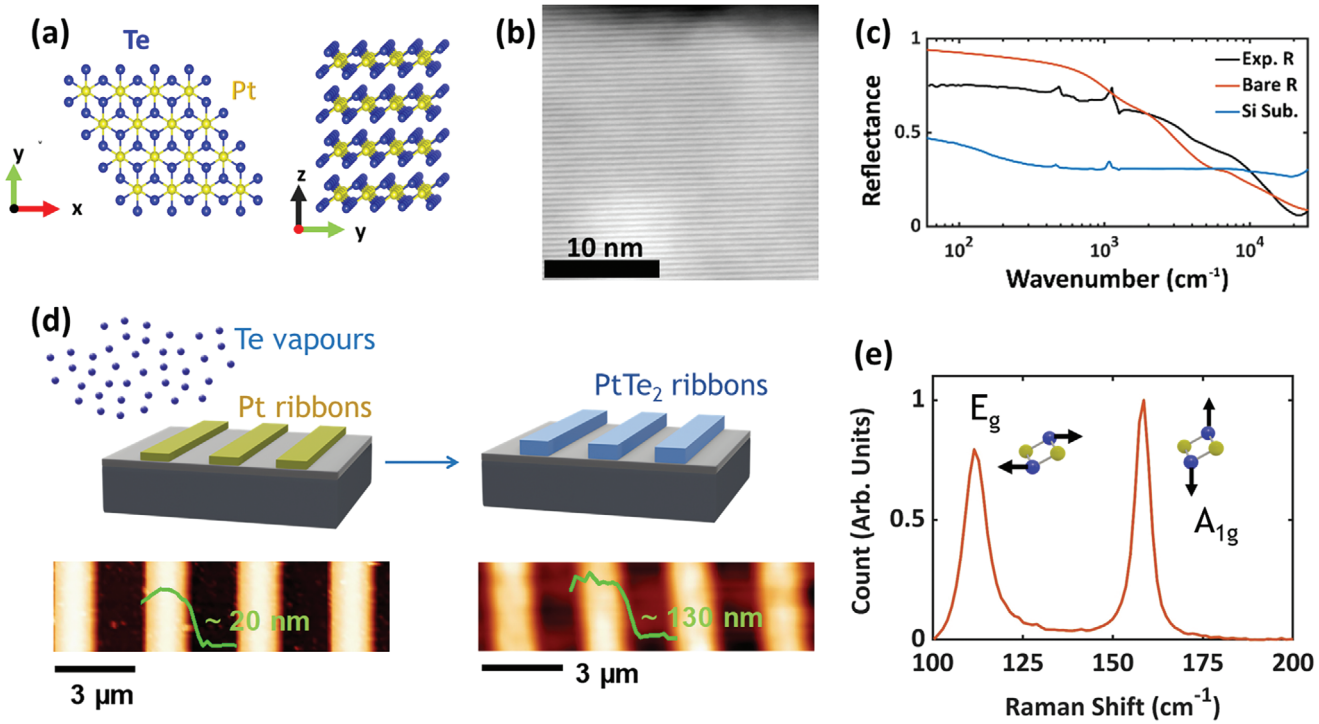

Figure 1. a) $PtTe_2$ crystal structure sketch on the *xy*- and *yz*-planes. b) HAADF-STEM cross-sectional imaging of the non-patterned $PtTe_2$ layers. The HAADF-STEM analysis is sensitive to the atomic number of the mapped elements; the image reflects the atomic arrangement of the heavier Pt atoms in parallel planes along the (001) direction as sketched in panel a). c) Reflectance from THz to VIS of an unpatterned film (black-curve) and of the Si substrate (blue-curve). The bare $PtTe_2$ reflectance (red-curve) is obtained through the RefFIT fitting software (see main text) d) Scheme of the synthesis of the $PtTe_2$ micro-ribbon array. The pre-deposited Pt microribbon arrays are tellurized at $T = 550$ °C. Atomic force microscopy (AFM) topographies of the micro-ribbon array before (left, bottom) and after (right, bottom) the tellurization process. The green traces are the corresponding height profiles. e) Characteristic in-plane (E_g) and out-of-plane (A_{1g}) Raman modes of the trigonal 1T phase of $PtTe_2$. A sketch of these vibrational modes is shown in the inset where yellow and blue spheres are Pt and Te atoms, respectively.

micro-ribbon array is preserved after the tellurization stage, while the ribbon height expands from ≈20 nm in the pristine Pt film to ≈130 nm in the tellurized film due to a reaction-triggered expansion of the crystalline arrangement. The AFM characterization of this feature can be seen in Section 2 and Figure S2 (Supporting Information).[42] In addition, the $PtTe_2$ formation is confirmed by the Raman spectrum of the as-grown material displaying two well-defined peaks at frequencies of 111 and 158 cm^{-1} associated with the (in-plane) E_g and (out-of-plane) A_{1g} vibrational modes of the trigonal (1T) phase of $PtTe_2$, respectively (see Figure 1e).[43,44]

Therefore, $PtTe_2$ micro-ribbon arrays (**Figure 2a**) with varying widths W and period 2 W in the microscale ($W = 20$, 15, 8, 5, 3, and 1.5 μm) were fabricated to select a discrete set of suitable values of the SPP wavevector $q = \pi/W$. SPP excitations have been studied by measuring the reflectance at nearly normal incidence of patterned films. When the electric field is parallel to the ribbons (Figure 2b), one measures the Drude response of the film-on-substrate renormalized by the patterning.[10] This effect is evident for the $W = 1.5$ μm array where the Drude contribution is particularly strong and resembles that of the non-patterned film. The opposite situation is observed in case of $W = 20$ μm where the parallel reflectance is strongly reduced with respect to the as-grown film (see Figure 1c). On the first spectrum of Figure 2b the SiO_2 phonon absorption peaks are highlighted with red circles, as already observed in the as-grown film. Figure 2c shows the reflectance spectra obtained with polarization perpendicular to the ribbons. Here we observe the SPP peaks both at the $PtTe_2$-silicon and at the $PtTe_2$–air interfaces. In particular, for a given wavevector q, $PtTe_2$-silicon SPP is lower in frequency with respect to the corresponding SPP at the $PtTe_2$–air interface.[10]

The SPP features (both at the $PtTe_2$-silicon and at the $PtTe_2$–air interfaces) are superimposed to a reflectance background, modulated by the phonon absorption peaks. Therefore, the SPP intensity strongly depends on its superposition with this background. In order to assign the peaks in Figure 2c to SPP excitations at a specific interface (i.e., $PtTe_2$/substrate or $PtTe_2$/air), we also performed an electromagnetic (finite element) simulation based on the COMSOL Multiphysics software (see Methods). The comparison among experimental SPP reflectance (blue line) and simulation (orange line) is shown in **Figure 3a,b**, for $W = 20$ μm and $W = 8$ μm, respectively.

As inputs to these simulations, we used the experimental optical conductivities of both the non-patterned $PtTe_2$ film and substrate as extracted from the fit to their reflectance spectra (Figure 1c). Experiment and simulation display a good agreement, allowing us (see below and Supporting Information), to assign, for each W, the low-frequency SPP excitations to the $PtTe_2$-silicon interface and the high-frequency one to the $PtTe_2$–air interface. In the $W = 8$ μm array, the experimental SPP

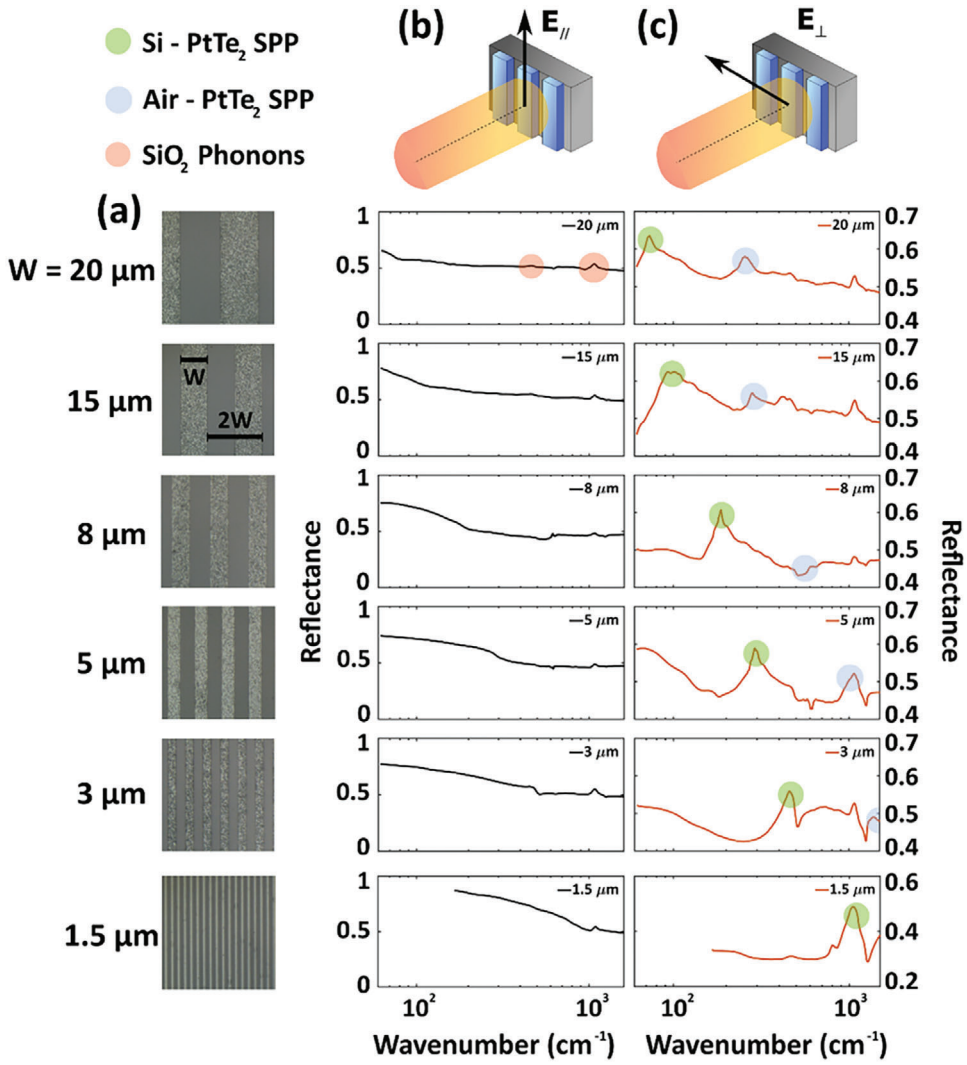

Figure 2. a) Optical microscope images of the five patterned films with different widths W and periodicity $2W$. b) Reflectance of the six patterned films, for the light polarization parallel to the ribbons. In this case, one measures a Drude response like in the unpatterned film (see Figure 1c), whose intensity is renormalized by the patterning. We identify in the upper first panel the two main phonons of SiO_2 (red circles) which are present in all measurements. c) Reflectance of the six patterned films, for the light polarization perpendicular to the ribbons. This optical configuration instead, is sensitive to SPP excitations. The position of the two SPP features is highlighted in each spectrum of column c). The lower frequency peak corresponds to the SPP excitation at the $PtTe_2$–silicon interface (green circles), while at higher frequency the SPP excitation is related to the $PtTe_2$–air interface (blue circles).

feature at the $PtTe_2$–air interface (blue line) is barely visible in comparison to the simulation (orange line). Its characteristic frequency (≈480 cm^{-1}) is partially superimposed to the SiO_2 phonon absorption at about 500 cm^{-1}. In similar cases,[18] this frequency resonance may induce a Fano interaction between the SPP and the phonon inducing a modification of the SPP spectral shape. This interaction is not taken into account in the simulation model. On the other hand, although the minimum in the experimental reflectance data at ≈150 cm^{-1} is not well described by the simulation, the peak frequency associated with the SPP mode (at the $PtTe_2$–substrate interface) is well captured by the model as follows from the dispersion curve plotted in Figure 3c.

To investigate the SPP dispersion as a function of the wavevector q, we estimated the SPP frequency ω_{spp} for the $PtTe_2$–Si interface from both experimental and simulated spectra (the same procedure has been applied for the $PtTe_2$–air interface, see Supporting Information). In particular, the ω_{spp} frequency can be deduced by $R(\omega)$ data through the zero-crossing of its second derivative (see also Section 5, Supporting Information).[10] In Figure 3c, we plot the SPP dispersion at the $PtTe_2$–Si interface: The solid blue circles correspond to the experimental frequencies while the red crosses to the simulated ones. These experimental and simulated frequencies are compared, within a thin film model, with the theoretical values given by the poles of the Fresnel reflection coefficient:

$$r(\omega) = \frac{\epsilon_S(\omega)\, q_\perp - q'_\perp + \sigma_f(\omega)\, dZ_0 q'_\perp}{\epsilon_S(\omega)\, q_\perp + q'_\perp + \sigma_f(\omega)\, dZ_0 q'_\perp} \quad (1)$$

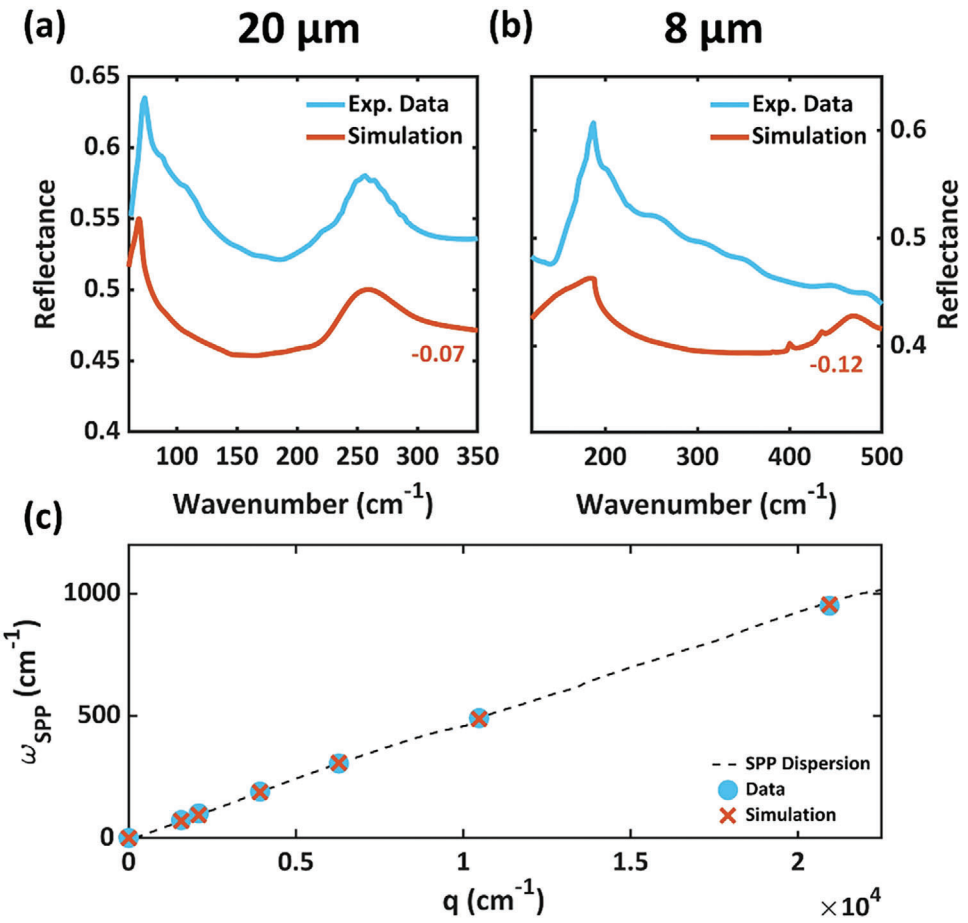

Figure 3. Comparison among experimental (blue lines) and simulated (orange lines) reflectance of $PtTe_2$ ribbon arrays with $W = 20\,\mu m$ (a) and $W = 8\,\mu m$ (b). Simulated spectra have an offset of −0.07 and −0.12, to better compare them with the experimental ones. c) SPP dispersion curve. Blue dots correspond to experimental SPP frequencies, while the black dashed line corresponds to the model (Equation 2, main text). SPP frequencies obtained with COMSOL Multiphysics simulations are reported with red crosses. Simulated and modeled data are in excellent agreement with the measured SPP frequencies as a function of the wavevector $q = \pi/W$.

where $\epsilon_S(\omega)$ and $\sigma_f(\omega)$ are the dielectric function of silicon, and the optical conductivity of the $PtTe_2$ film, respectively. d is the thickness of the film ($d = 130$ nm in our case, see Figure 1d), $Z_0 = 377\ \Omega$ is the free space impedance, and $q_\perp$ and $q'_\perp$ are the incident and transmitted (inside the film) wavevectors of the light, perpendicular to the film surface.

From the poles of Equation (1), we obtain the expected SPP dispersion (Equation (2)):

$$q_{||}^2(\omega) = \epsilon_S(\omega)\, q_0^2 \left[1 - \frac{\epsilon_S(\omega)}{\left(1 + \sigma_f(\omega)\, Z_0\right)^2}\right] \tag{2}$$

In Figure 3c we thus represent the SPP dispersion determined by this method (black dashed line). We find out an excellent agreement among experimental data, simulation, and model within the experimental uncertainty. In particular, since ω_{SPP} increases linearly with q, the wavevector range here investigated is fully consistent with the polariton regime.

Due to the SPP excitations, an electric field enhancement can be observed near the ribbon edges at both the substrate and air interfaces, giving rise to a hot spot volume accessible for surface-enhanced infrared spectroscopy (SEIRA) based sensing applications.[13] To better understand this behavior, we estimated the electric field spatial distribution map for all the ribbon arrays from the simulation data. The SPP field enhancement $FE = |E_{SPP}/E_i|$, is defined as the electric field at the SPP resonance E_{SPP} over the incident field E_i, both of which being integrated over a circular area surrounding the ribbon section.[10] FE, represented in panel a) of **Figure 4** by blue dots, is extracted from the field spatial distribution maps. Two of these maps are shown in Figure 4c and d for the arrays with $W = 5\,\mu m$ and $W = 1.5\,\mu m$. The FE ($\approx 10^4$) value confirms the potential of $PtTe_2$-based ribbon arrays for SEIRA applications in the THz and IR regime.

To further confirm the importance for SEIRA applications of SPP excitations based on type-II Dirac $PtTe_2$ system, the electric field distribution along the z-axis (e.g., perpendicular to the ribbon plane) has been simulated through COMSOL Multiphysics (see Figure 4b, blue line) showing a strong enhancement near the

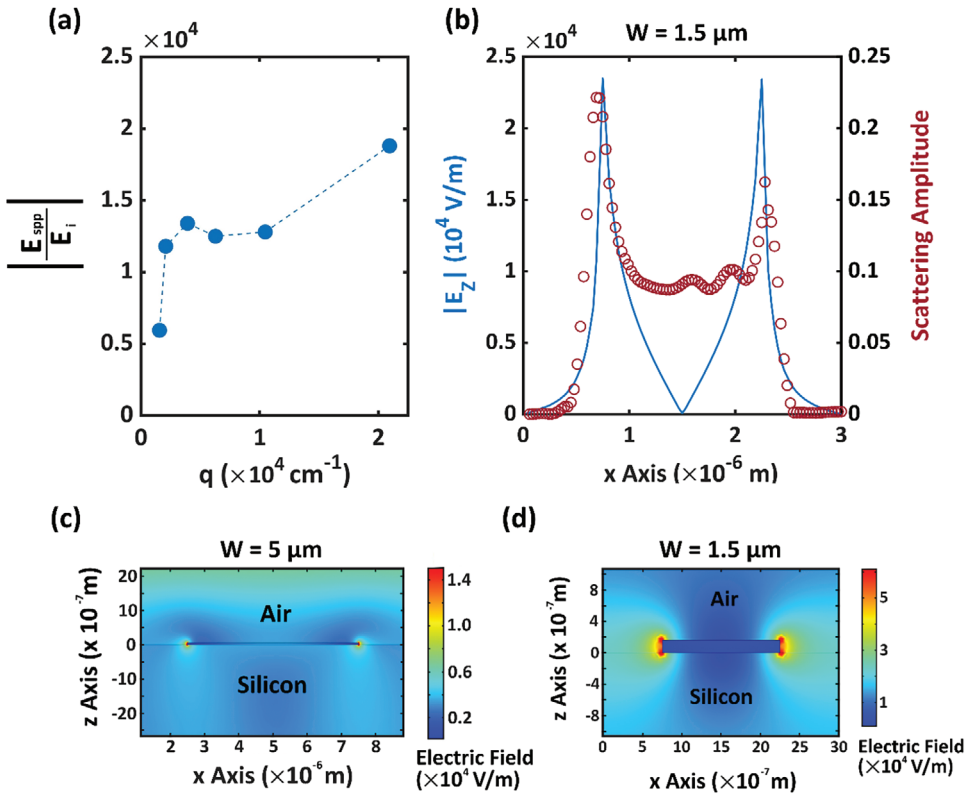

Figure 4. a) Field enhancement $|E_{SPP}/E_i|$ plotted versus the experimental wavevector q. Here, E_{SPP} is the electric field at the plasmonic resonance, while E_i is the incident field. b) Comparison between the modulus of the electric field component perpendicular to the sample surface (blue line), obtained through the finite element simulations, and the experimental scattered amplitude (red dots), obtained from the near field measurements, for the sample with $W = 1.5$ μm. The experimental strong increase of the electric field at the ribbon edges is in very good agreement with the simulation. Electric field 2D map obtained from the simulations of the section of a $W = 5$ μm (c) and a $W = 1.5$ μm (d) ribbon, with the silicon substrate below and the air above. The electric field is mainly confined at the edges of the ribbon structure. The field enhancement is calculated by integrating the electric field over a circular area with a diameter equal to the full width half maximum (FWHM) of the electric field modulus.

ribbon edge. This enhancement can be experimentally measured through a scattering-type scanning near-field optica microscopy (s-SNOM), see methods and Supporting Information. Indeed, an s-SNOM is able to probe the near-field infrared scattered signal, with a spatial resolution well below the diffraction limit. The near-field signal is related to the out-of-plane local electric field E_Z (for details see Experimental Section and Section 7, Supporting Information). We performed s-SNOM measurements in the IR regime on the $W = 1.5$ μm sample both in resonance with its SPP excitation (at 950 cm^{-1}) and out-of-resonance at 1150 cm^{-1}. The spatially resolved near-field IR maps are shown in Figure S8 (Supporting Information) both in-resonance (left part of the Figure) and out-of-resonance (right-part of the Figure). From the map at 950 cm^{-1} we obtained the near-field profile represented (with red-dots) in Figure 4b. We notice a very good match between the experimental and simulation data, showing a strong electric field enhancement at the ribbon edges.

3. Conclusion

Following up graphene applications to smart optical devices,[12] linearly dispersive electronic bands characterized by high-mobility charge-carrier at room temperature can also be found in topological materials, suggesting their disruptive technological potentiality for novel optoelectronic applications particularly in photonics and plasmonics.[16] In this work, we fabricated microribbon arrays of $PtTe_2$ nanoscale films in the 1T structural phase which displays a type-II Dirac topological semimetal character. Aiming to study the electrodynamics of optically excited carriers in the $PtTe_2$ arrays, we have shown that films with different ribbon width W and periodicity $2W$, sustain Surface Plasmon Polariton excitations with energy/momentum dispersion in the THz and IR spectral region thereby bringing evidence of the type II Dirac semimetal character. From the bulk of these observations, we demonstrate plasmonic resonance tuning in the THz and IR spectrum by geometrical pattern design, and we expect that the reported geometrical tunability of Dirac Surface Plasmon Polaritons can be alternately achieved by using an electrostatic gating and/or an ultrafast optical pulse. We showed with simulations and s-SNOM Near Field measurements the strong Field Enhancement ($\approx 10^4$) that occurs at the edge of the micro-stripes, confirming the potential of the $PtTe_2$ arrays for SEIRA applications.

We finally emphasized that $PtTe_2$ is configured in the form of a synthetic ultra-thin film on a Si-based substrate that readily enables the technology transfer to read-out integrated circuit

platform thereby empowering concrete applications in photonics and plasmonics.

4. Experimental Section

Synthesis, Patterning and Characterization of PtTe2 Film: To prepare the samples, SiO_2/Si substrates are heated to 120 °C to remove moisture and carbon-related residue. The micro-stripe arrays are then fabricated by defining the pattern through optical lithography, using the Tabletop Maskless Aligner μm MLA (Heidelberg GmbH), over the whole sample area. The substrates are spin-coated with a layer of UV-sensitive resist with a thickness of ≈1 μm. Stripe patterns are written into the resist by exposure to light. The patterned resist serves as a mask for the 20 nm-thick Pt evaporation by DC magnetron sputtering and subsequent lift-off. The patterned samples (Figure S1, Supporting Information) are put in a double furnace chemical vapor deposition system (PlanarTECH Ltd) for the tellurization processing. Te powder (150 mg; 99.997%, Sigma-Aldrich, Darmstadt, Germany) is placed in a ceramic boat (crucible 1) in the middle of upstream and a pre-patterned sputtered Pt on SiO_2/Si serves as substrate (Figure S1, Supporting Information) faced up with tilted orientation in a covered quartz boat (crucible 2) in the downstream (Figure S1, Supporting Information). At the growth stage, the upstream and downstream temperatures reach 625 and 550 °C, respectively. As a carrier gas, Ar/4%H_2 flows at 100 sccm and transports the evaporated Te powder toward the Pt-patterned substrate boat to activate the reaction between Te and Pt resulting in $PtTe_2$. The morphological characterization of the sample is performed in tapping mode using a commercial AFM (Bruker Corp., Dimension edge) equipped with an ultra-sharp silicon tip (radius ≈ 10 nm). The topographical analysis is carried out by using WSxM software. Micro-Raman spectroscopy is used to characterize the sample structure after tellurization by means of a Renishaw Ltd InVia analyzer equipped with a solid-state laser source of excitation wavelength 514 nm (2.41 eV) in a backscattering configuration. The laser power is kept below 1 mW to avoid sample damage during the measurements.

To obtain the lamellae for the HADDF-STEM analysis, the samples are prepared by means of a focused ion beam (FIB). The lamellae preparation is performed using a Thermo-Fischer Helios G4 FIB. In all the cases, particular care is taken to limit the heating and ballistic effects of ion irradiation on $PtTe_2$ film during the final ion milling steps.

After the FIB, lamellae are investigated by means of scanning transmission electron microscopy (STEM) techniques. The images were performed with a Thermo-Fischer Themis Z G3 aberration-corrected transmission electron microscope equipped with an electron gun monochromator operating at 200 kV acceleration voltage. The EDX elemental maps and profile analyses are acquired with Dual-X Thermo Fisher energy dispersive X-rays.

Optical Measurements: Optical measurements in the THz-IR range are carried out with a Bruker Vertex 70v spectrometer coupled with a Hyperion 1000 microscope, scanning from 60 cm^{-1} up to 8000 cm^{-1}. In the IR-UV range, the reflectance was measured with a JASCO V770 spectrometer, from 300 nm (3.3×10^4 cm^{-1}) up to 3200 nm (3125 cm^{-1}). A set of THz/UV polarizers are used to control the electric field direction with respect to the ribbon array pattern. The $PtTe_2$ and Si optical data are analyzed with the RefFIT software,[40] in order to extract the real and imaginary parts of both the dielectric function and optical conductivity. By means of a Kramers–Kronig-constrained simultaneous fitting of reflectance $R(\omega)$ and transmittance $T(\omega)$ of the substrate, the real (n) and the imaginary (k) part of the refractive index are determined for Si. n and k are used as input parameters in the RefFIT multi-layer model to extract the $PtTe_2$ optical parameters.

Simulation: A finite-element method, implemented by means of COMSOL Multiphysics, is used to obtain the numerical simulations of the reflectance of films in the frequency range between 60 and 3000 cm^{-1}. The ribbon arrays are simulated applying periodic boundary conditions to a unit cell of period $p = 2\ W$, for width of $W = 20$, 15, 8, 5, 3, and 1.5 μm. As the input of the numerical simulation, the complex refractive indexes of $PtTe_2$ and Si are used as obtained from the RefFIT data analysis of the non-patterned film and bare substrate, respectively.

Scattering-Type Scanning Near-Field Optical Microscopy Measurements: To conduct nano-resolved IR microscopy and AFM measurements, metallic tips (ARROW-NcPt from Nano World, Matterhorn, Switzerland) with a diameter of ≈20 nm are utilized, with 285 kHz of nominal resonance frequency, and a force constant of 42 N m^{-1}. The measurements are conducted in tapping mode at a tapping frequency Ω of 267.9 kHz, with an IR QCL tunable laser operating at 950 and 1150 cm^{-1}. Detection of the infrared signal is allowed by a nitrogen-cooled mercury cadmium tellurium detector. The phase and amplitude of the IR signal are directly acquired through the Neaspec acquisition software, Neascan, employing lock-in demodulation of the interference signal at the third harmonic of the cantilever oscillation frequency, with a silicon substrate serving as a reference. Post-processing of the data is carried out using Neaplotter (Neaspec), incorporating a phase correction filter to accommodate minor phase variations of the IR laser.

Supporting Information

Supporting Information is available from the Wiley Online Library or from the author.

Acknowledgements

This publication was supported by the European Union (EU) under the Italian National Recovery and Resilience Plan (NRRP) of Next Generation EU partnership PE0000023-NQSTI and "Telecommunications of the Future" (PE00000001 – program "RESTART", Structural Project DREAMS), and by the Ministero dell'Università e della Ricerca (MUR), call PRIN 2020, project "PHOtonics Terahertz devices based on topological materials" ("PHOTO"), grant no. 2020RPEPNH.

Conflict of Interest

The authors declare no conflict of interest.

Author Contributions

All authors contributed extensively to the work presented in this paper. S.M., A.M., and S.L. designed the experiment. S.L. and A.M. supervised the work and the research program. A.M. and Chr.M. designed the layout of the materials. S.G., P.P.T., A.L., and C.M. prepared the substrate and performed the materials growth. E.B., P.P.T., and S.G. performed the Raman spectroscopy. C.M., E.B., and Chr.M. fabricated the stripe patterns. S.G. and Chr.M. performed atomic force microscopy. O.P. and S.G. simulated the band structure of the material. S.M. and L.M. developed the theoretical model. S.T. developed and performed the numerical simulations. S.M., L.M., M.C.P., and A.D. took the optical images, performed the optical measurements, and analyzed the data. D.C., A.S., and P.T. performed the STEM measurements. V.S. and M.Z. performed the s-SNOM measurements. S.M., L.M., and S.L. prepared the original draft. All authors reviewed the manuscript. All authors have read and agreed with the published version of the manuscript.

Data Availability Statement

The data that support the findings of this study are available from the corresponding author upon reasonable request.

Keywords

metamaterials, photonics, plasmonics, $PtTe_2$, topological materials

Received: January 11, 2024
Revised: April 18, 2024
Published online: May 22, 2024

[1] S. A. Maier, *Plasmonics: Fundamentals and Applications*, Springer Science & Business Media, New York, NY, USA, **2007**.
[2] F. Piccirilli, F. Tardani, A. D'Arco, G. Birarda, L. Vaccari, S. Sennato, S. Casciardi, S. Lupi, *Nanomaterials* **2021**, *11*, 1103.
[3] O. Limaj, S. Lupi, F. Mattioli, R. Leoni, M. Ortolani, *Appl. Phys. Lett.* **2011**, *98*, 091902.
[4] O. Limaj, F. D'Apuzzo, A. Di Gaspare, V. Giliberti, F. Domenici, S. Sennato, F. Bordi, S. Lupi, M. Ortolani, *J. Phys. Chem. C* **2013**, *117*, 19119.
[5] F. D'Apuzzo, M. Esposito, M. Cuscunà, A. Cannavale, S. Gambino, G. E. Lio, A. De Luca, G. Gigli, S. Lupi, *ACS Photonics* **2018**, *5*, 2431.
[6] O. Limaj, F. Giorgianni, A. Di Gaspare, V. Giliberti, G. de Marzi, P. Roy, M. Ortolani, X. Xi, D. Cunnane, S. Lupi, *ACS Photonics* **2014**, *1*, 570.
[7] S. M. Anlage, *J. Opt.* **2010**, *13*, 024001.
[8] S. Macis, M. C. Paolozzi, A. D'Arco, L. Tomarchio, A. Di Gaspare, S. Lupi, *Appl. Sci.* **2022**, *12*, 10242.
[9] M. Liu, H. Y. Hwang, H. Tao, A. C. Strikwerda, K. Fan, G. R. Keiser, A. J. Sternbach, K. G. West, S. Kittiwatanakul, J. Lu, S. A. Wolf, F. G. Omenetto, X. Zhang, K. A. Nelson, R. D. Averitt, *Nature* **2012**, *487*, 345.
[10] S. Macis, L. Tomarchio, S. Tofani, F. Piccirilli, M. Zacchigna, V. Aglieri, A. Toma, G. Rimal, S. Oh, S. Lupi, *Commun. Phys.* **2022**, *5*, 145.
[11] F. H. L. Koppens, D. E. Chang, F. J. García de Abajo, *Nano Lett.* **2011**, *11*, 3370.
[12] T. Low, P. Avouris, *ACS Nano.* **2014**, *8*, 1086.
[13] F. D'Apuzzo, A. R. Piacenti, F. Giorgianni, M. Autore, M. C. Guidi, A. Marcelli, U. Schade, Y. Ito, M. Chen, S. Lupi, *Nat. Commun.* **2017**, *8*, 14885.
[14] S. Macis, M. C. Paolozzi, A. D'Arco, F. Piccirilli, V. Stopponi, M. Rossi, F. Moia, A. Toma, S. Lupi, *Nanoscale* **2023**, *15*, 16002.
[15] N. Kumar, S. N. Guin, K. Manna, C. Shekhar, C. Felser, *Chem. Rev.* **2021**, *121*, 2780.
[16] S. Lupi, A. Molle, *Appl. Mater. Today* **2020**, *20*, 100732.
[17] L. Tomarchio, S. Mou, L. Mosesso, A. Markou, E. Lesne, C. Felser, S. Lupi, A. C. S. Appl, *Electron. Mater.* **2023**, *5*, 1437.
[18] P. Di Pietro, M. Ortolani, O. Limaj, A. Di Gaspare, V. Giliberti, F. Giorgianni, M. Brahlek, N. Bansal, N. Koirala, S. Oh, P. Calvani, S. Lupi, *Nat. Nanotechnol.* **2013**, *8*, 556.
[19] M. Autore, H. Engelkamp, F. D'Apuzzo, A. D. Gaspare, P. D. Pietro, I. L. Vecchio, M. Brahlek, N. Koirala, S. Oh, S. Lupi, *ACS Photonics* **2015**, *2*, 1231.
[20] F. Giorgianni, E. Chiadroni, A. Rovere, M. Cestelli-Guidi, A. Perucchi, M. Bellaveglia, M. Castellano, D. Di Giovenale, G. Di Pirro, M. Ferrario, R. Pompili, C. Vaccarezza, F. Villa, A. Cianchi, A. Mostacci, M. Petrarca, M. Brahlek, N. Koirala, S. Oh, S. Lupi, *Nat. Commun.* **2016**, *7*, 11421.
[21] P. Di Pietro, *Phys. Rev. Lett.* **2020**, *124*, 226403.
[22] N. P. Armitage, *Rev. Mod. Phys.* **2018**, *90*, 015001.
[23] M. S. Bahramy, O. J. Clark, B.-J. Yang, J. Feng, L. Bawden, J. M. Riley, I. Marković, F. Mazzola, V. Sunko, D. Biswas, S. P. Cooil, M. Jorge, J. W. Wells, M. Leandersson, T. Balasubramanian, J. Fujii, I. Vobornik, J. E. Rault, T. K. Kim, M. Hoesch, K. Okawa, M. Asakawa, T. Sasagawa, T. Eknapakul, W. Meevasana, P. D. C. King, *Nat. Mater.* **2018**, *17*, 21.
[24] A. A. Soluyanov, D. Gresch, Z. Wang, Q. Wu, M. Troyer, X. Dai, B. A. Bernevig, *Nature* **2015**, *527*, 495.
[25] H. Huang, S. Zhou, W. Duan, *Phys. Rev. B* **2016**, *94*, 121117.
[26] J. Hofmann, S. Das Sarma, *Phys. Rev. B* **2016**, *93*, 241402.
[27] M. Yan, H. Huang, K. Zhang, E. Wang, W. Yao, K. Deng, G. Wan, H. Zhang, M. Arita, H. Yang, Z. Sun, H. Yao, Y. Wu, S. Fan, W. Duan, S. Zhou, *Nat. Commun.* **2017**, *8*, 257.
[28] K. J. A. Ooi, Y. S. Ang, Q. Zhai, D. T. H. Tan, L. K. Ang, C. K. Ong, *APL Photonics* **2018**, *4*, 034402.
[29] H. Xu, J. Wei, H. Zhou, J. Feng, T. Xu, H. Du, C. He, Y. Huang, J. Zhang, Y. Liu, H.-C. Wu, C. Guo, X. Wang, Y. Guang, H. Wei, Y. Peng, W. Jiang, G. Yu, X. Han, *Adv. Mater.* **2020**, *32*, 2000513.
[30] H. Xu, C. Guo, J. Zhang, W. Guo, C.-N. Kuo, C. S. Lue, W. Hu, L. Wang, G. Chen, A. Politano, X. Chen, W. Lu, *Small* **2019**, *15*, 1903362.
[31] J. He, H. Lu, L. Tao, Y. Zhao, Z. Zheng, B. Zhou, *J. Mater. Chem. C* **2022**, *10*, 5124.
[32] J. Li, S. Kolekar, M. Ghorbani-Asl, T. Lehnert, J. Biskupek, U. Kaiser, A. V. Krasheninnikov, M. Batzill, *ACS Nano* **2021**, *15*, 13249.
[33] G. Y. Guo, W. Y. Liang, *J. Phys. C: Solid State Phys.* **1986**, *19*, 995.
[34] M. B. Cortie, M. D. Arnold, V. J. Keast, *Adv. Mater.* **2020**, *32*, 1904532.
[35] O. J. Clark, F. Mazzola, I. Marković, J. M. Riley, J. Feng, B.-J. Yang, K. Sumida, T. Okuda, J. Fujii, I. Vobornik, T. K. Kim, K. Okawa, T. Sasagawa, M. S. Bahramy, P. D. C. King, *Electron. Struct.* **2019**, *1*, 014002.
[36] A. Politano, G. Chiarello, B. Ghosh, K. Sadhukhan, C.-N. Kuo, C. S. Lue, V. Pellegrini, A. Agarwal, *Phys. Rev. Lett.* **2018**, *121*, 086804.
[37] I. Pelayo, D. Bergner, A. J. Williams, J. Qi, Mahfuzun Nabi, W. L. B. Huey, L. Moreschini, Z. Deng, J. Denlinger, A. Lanzara, W. Windl, J. Goldberger, C. Ojeda-Aristizabal, arXiv:2312.15371.
[38] G. Kliche, *J. Solid State Chem.* **1985**, *56*, 26.
[39] G. Lucovsky, M. J. Mantini, J. K. Srivastava, E. A. Irene, *J. Vac. Sci. Technol., B: Microelectron. Nanometer Struct.–Process., Meas., Phenom.* **1987**, *5*, 530.
[40] A. B. Kuzmenko, *Rev. Sci. Instrum.* **2005**, *76*, 083108.
[41] P. P. Tummala, S. Ghomi, C. S. Casari, C. Martella, A. Lamperti, A. Molle, *Adv. Mater. Interfaces* **2023**, *10*, 2200971.
[42] X.-W. Tong, Y.-N. Lin, R. Huang, Z.-X. Zhang, C. Fu, D. Wu, L.-B. Luo, Z.-J. Li, F.-X. Liang, W. Zhang, *ACS Appl. Mater. Interfaces* **2020**, *12*, 53921.
[43] J. Guo, Z. Luo, J. Liao, Y. Nie, Q. Xia, R. Xiong, G. Guo, *J. Appl. Phys.* **2021**, *130*, 233901.
[44] S. Hao, J. Zeng, T. Xu, X. Cong, C. Wang, C. Wu, Y. Wang, X. Liu, T. Cao, G. Su, L. Jia, Z. Wu, Q. Lin, L. Zhang, S. Yan, M. Guo, Z. Wang, P. Tan, L. Sun, Z. Ni, S.-J. Liang, X. Cui, F. Miao, *Adv. Funct. Mater.* **2018**, *28*, 1803746.